Astronomy & Astrophysics

Variations in the intermediate wind region of the blue supergiant 55 Cygni[*]

L. S. Cidale[1,2,**], M. Haucke[3], M. L. Arias[1,2,**], M. Kraus[4], F. Campuzano Castro[1], R. O. J. Venero[1,2,**], L. Mercanti[1,2,***], M. Curé[5], and A. Granada[6,**]

[1] Departamento de Espectroscopía, Facultad de Ciencias Astronómicas y Geofísicas, Universidad Nacional de La Plata, Paseo del Bosque s/n, B1900FWA La Plata, Buenos Aires, Argentina
e-mail: lydia@fcaglp.unlp.edu.ar
[2] Instituto de Astrofísica de La Plata, CONICET-UNLP, Paseo del Bosque s/n, B1900FWA La Plata, Buenos Aires, Argentina
[3] Facultad de Ingeniería, Universidad Nacional de La Plata, Av. 1 No. 750, B1900TAG La Plata, Buenos Aires, Argentina
[4] Astronomical Institute, Czech Academy of Sciences, Fričova 298, 251 65 Ondřejov, Czech Republic
[5] Instituto de Física y Astronomía, Facultad de Ciencias, Universidad de Valparaíso, Av. Gran Bretaña 1111, Casilla 5030, Valparaíso, Chile
[6] Universidad Nacional de Rio Negro, Sede Andina, CITECCA. Anasagasti 1461, San Carlos de Bariloche, Argentina

ABSTRACT

Context. The quantitative near-infrared (NIR) spectroscopic synthesis is an important technique for determining wind properties of massive stars. The Brα line is an excellent mass-loss tracer and provides valuable information on the physical conditions of intermediate-wind regions. The knowledge of the wind properties gained by studying the NIR lines could provide extra ingredients to the theory of line-driven winds, mainly because the standard theory does not predict observed properties of blue supergiants, such as high values for the β parameter ($\beta > 2$), low terminal velocities, and mass-loss variability.
Aims. We seek to enhance our understanding of the wind properties of B supergiants. To this end, we propose analysing their NIR spectra over different epochs to study wind variability and its connection with phenomena arising from regions close to the photosphere.
Methods. We present the first sets of multi-epoch high-resolution K- and L-band spectra of 55 Cyg acquired with the Gemini Near-InfraRed Spectrograph (GNIRS). We measured line equivalent widths and modelled the Brα line to derive (unclumped) mass-loss rates. Synthetic line profiles were computed for a homogeneous spherical wind by solving the radiative transfer equations in the co-moving frame for a multi-level atom in non-local thermodynamic equilibrium (NLTE).
Results. We observe variations in the spectral lines originating in the upper photosphere and the wind. The perturbations, on average, have periods of ~13 and ~23 days; the latter is similar to that found previously from optical data (22.5 days). The NIR lines observed in 2013 are described with the same wind structure used to model a quasi-simultaneous observation in Hα. By contrast, from observations taken in 2015, we derived a higher mean mass-loss rate. Variations in the mass-loss rate are also detected within a few weeks. Interestingly, we find that the profile shape of the Hu₁₄ line sets constraints on the mass loss. Moreover, we find the Mg II doublet in emission, which suggests a tenuous circumstellar gas ring or shell.
Conclusions. The variability detected in the NIR H emission lines of 55 Cyg is related to changes in the mass-loss rate, which doubled its value between 2013 and 2015. Furthermore, the short-term variability (within three weeks) in the spectral lines and mass loss supports the hypothesis of strange-mode oscillations. This pilot project demonstrates the importance of comprehensive monitoring of blue supergiants' variability to deeply understand the physical properties of their stellar winds and the role of pulsations in recurrently enhancing mass loss.

Key words. supergiants – stars: mass-loss – stars: winds, outflows – stars: individual: 55 Cyg

1. Introduction

Massive stars can expel a large amount of mass as stellar winds. The mass-loss rate is one of the most important ingredients for calculating the evolution and fate of these stars (De Loore et al. 1977; Chiosi & Maeder 1986; Puls et al. 2008; Ekström et al. 2012; Georgy et al. 2012; Georgy 2012). Moreover, precise values are needed because of the observed occasionally enhanced mass-loss rates within specific evolutionary stages. Depending on the total mass the star lost over the entire lifetime, the final stages of massive stars could be very different because the star might end its life as a neutron star rather than as a black hole (Eldridge & Tout 2004; Smith 2014; Meynet et al. 2015). The

mass-loss rate not only defines the evolution of the object per se, but it also alters the chemical and dynamical evolution of galaxies, providing conditions to trigger the formation of new stars. The B-type supergiants (BSGs) constitute one such group of massive stars with strong winds. These objects are in either the pre- or post-red supergiant (RSG) evolutionary stage (Ekström et al. 2012), and their outflowing material is, in principle, mainly described by the theory of line-driven winds (Lucy & Solomon 1970; Castor et al. 1975; Pauldrach et al. 1986; Friend & Abbott 1986).

In the optical spectral region, the Hα line is the prototypical mass-loss diagnostics in OB supergiants. Nevertheless, quite often, to match this line, it is necessary to consider a low-gradient velocity field described by a β law with $\beta > 2$ (Markova et al. 2008; Haucke et al. 2018) instead of the typical value $\beta \sim 1$ that results from line-driven wind theory (m-CAK, Pauldrach et al. 1986) when employing the usual force-multiplier parameters (i.e. Abbott 1982). These sets of line-force parameters, mainly the low value of δ, lead to a fast wind solution as opposed to another slow hydrodynamic solution obtained if δ were greater than ~0.26 (Curé et al. 2011; Venero et al. 2016). On the other hand, there is direct evidence for stochastic wind clumping in the hot wind of massive stars (Lépine & Moffat 2008) and, usually, homogeneous wind model predictions do not agree with either the observed mass-loss rates or the simultaneous fitting of the spectral lines in different wavelength bands (cf. Puls et al. 2008).

The BSGs also display photometric and spectroscopic variability in the optical range (Prinja et al. 2004; Lefever et al. 2007; Morel et al. 2004; Markova et al. 2008; Clark et al. 2010), often attributed to stellar pulsations, rotational modulation induced by weak magnetic fields, or instabilities of the ionisation structure of the wind (Kaufer et al. 1996). Strange mode pulsations have been proposed as a suitable mechanism to cause time-variable mass loss (Glatzel et al. 1999; Aerts et al. 2010; Kraus et al. 2015; Haucke et al. 2018). However, observational data for different epochs and spectral ranges are essential to establish such a link.

55 Cyg (B2.5/3 I) is of particular interest because of its strong variability, which is also present in the wind. Drastic changes in the shape and intensity of the Hα line profile were observed (Maharramov 2013). Moreover, Kraus et al. (2015) report multi-periodic variations in the radial velocity of optical photospheric lines covering periods from some hours up to about three weeks and variations in the mass-loss rate by a factor of 1.7–2.

Due to its large opacity, the Hα line is very sensitive to changes at the stellar surface and stellar-wind properties. However, the depth of the absorption component of the P-Cygni profile often shows a significant and persistent discrepancy with the synthetic one, which is noticeably weaker in the observed spectrum (Chesneau et al. 2010). Therefore, it might not be the best line to study correlations between photospheric perturbations (related to radial pulsations) and mass-loss behaviour. Najarro et al. (2011) suggested that the hydrogen lines in the near-infrared (NIR) domain provide more reliable information about the wind properties than those of the optical spectral region. These authors asserted that the Brα line, together with UV and optical lines, enables us to derive constraints on the (local) clumping factor (a parameter used to describe wind clumps, see Owocki et al. 1988). In addition, for objects with weak stellar winds, the Brα line is a more sensitive indicator of mass loss than Hα. Furthermore, as the NIR lines trace the intermediate and inner parts of the wind (Lenorzer et al. 2004; Najarro et al. 2011), they could bring additional information about the velocity

field and density structure of their line-forming regions (Barlow & Cohen 1977; Kudritzki & Puls 2000; Repolust et al. 2005).

For the present work, we carried out the first multi-epoch NIR spectroscopic observations of 55 Cyg performed at the Gemini North Observatory to analyse the wind structure, its variability, and its connection with phenomena that arise from regions close to the photosphere. We expect that IR lines are affected at least during short periods as perturbations pass through their formation regions.

The paper is organised as follows: Sect. 2 presents details on our NIR spectroscopic observations and data reduction. Sections 3 and 4 describe the analysis carried out on the spectra and the line-profile fitting procedure. Discussions on the wind structure and the evolutionary stage of the star are given in Sect. 5. Section 6 summarises our results.

2. Observations

High-resolution K- and L-band observations were obtained with the Gemini Near-InfraRed Spectrograph (GNIRS, Elias et al. 2006) at the Gemini North Observatory (Hawaii, US). The observations were taken in October 2013 and May and June 2015 under programmes GN-2013B-Q-108 and GN-2015A-Q-89 (PI: M. L. Arias). We used the long camera of 0.05″ pix^{-1}, a 0.10″ slit, and the 111 l/mm grating. This instrumental configuration gives a spectral resolving power of $R \sim 18\,000$. The K- and L-band spectra were centred at 2.166 μm (Brγ) and 4.05 μm (Brα), respectively. The observed epochs, the covered spectral range, and the signal-to-noise ratio (S/N) are listed in Table 1.

The sky thermal emission is significant in the NIR region and must be removed before the two-dimensional spectrum is summed along the cross-dispersed direction to obtain the one-dimensional spectrum (Hanson et al. 1996). An offset pattern ABBA (science-sky-sky-science) nodding along a four-pixel wide slit was applied to carry out this correction. Next, we independently subtracted the A-B and B-A pairs to remove the sky. Finally, the A-B and B-A pairs were aligned and co-added. The spectra reduction was performed using IRAF[1] software package tasks.

A second drawback arises when applying the telluric correction near the stellar H lines. To carry out the telluric correction, often the telluric standard stars of late B-type or early A-type 'dwarfs' are selected since their spectra have hydrogen lines as only intrinsic features. Here, the primary source of error comes from the appearance of the broad wing features present in the H lines of the telluric standard (Hanson et al. 1996). Different procedures were traditionally used to obtain a pure telluric spectrum and perform the telluric and instrumental corrections (see details in Hanson et al. 2005; Najarro et al. 2011). For our observing programme, we selected an A-type dwarf star observed near the science object in both time and sky positions (air mass). Once the stellar H lines were removed from the standard star, the programme star fluxes were divided by the fluxes of their related calibrators, using the 'telluric' IRAF task, cancelling out the effect of telluric features. The hydrogen lines of the standard stars were removed by fitting a Voigt profile to the observed line spectrum and subtracting it to get a purely telluric spectrum. As we were working with high-resolution spectra and a high S/N (> 250), the hydrogen line profiles of the A-type dwarf are pretty well distinguished from the well-defined sharp telluric lines and

---

[1] IRAF is distributed by the National Optical Astronomy Observatories, operated by the Association of Universities for Research in Astronomy, Inc., under contract to the National Science Foundation.

Table 1. Log of GNIRS observations.

Observation date [dd-mm-yy]	HJD [days]	Mean S/N in K band [2.13–2.19 µm]	Mean S/N in L band [4.00–4.09 µm]
26-10-2013	2456591	–	130
19-05-2015	2457162	194	134
07-06-2015	2457181	148	272
13-06-2015	2457187	266	162
19-06-2015	2457193	138	38
22-06-2015	2457196	185	224
24-06-2015	2457198	260	–
28-06-2015	2457202	204	275
29-06-2015	2457203	204	135

Notes. A dash means no spectrum was taken on that date.

could be satisfactorily removed. The wavelength calibration was also performed using the telluric lines. In summary, the basic reduction steps were subtraction of the AB pairs, flat fielding, wavelength calibration, and telluric correction.

3. Analysis and results

3.1. Line identification

We identified the lines observed in both the K- and L-band spectra and measured the equivalent widths (EWs) of either their absorption or emission components.

As an example, Fig. 1 shows K- and L-band spectra observed on June 22, 2015, with the most intense lines marked (based on the identifications provided by Morris et al. 1996; Clark & Steele 2000; Lenorzer et al. 2002; Kramida et al. 2018). These lines are mainly from H I and He I. Furthermore, noticeable emission features of Mg II at 2.137 µm and 2.143 µm are present in the K band. From this figure, we can also infer the complexity of the spectral regions around the Brγ (H I 4–7) and Brα (H I 4–5) lines. The former shows an incipient emission at its core and is blended with the He I line at 2.164 µm. The rest of the He I lines present in the K band are in absorption. The Brα line has an intricate profile that consists of a one-peaked emission superimposed over a broad photospheric absorption, which is, in turn, also blended with the emission line of He I 4.049 µm. This broad H absorption feature is present in the raw spectrum of the star before performing the telluric correction. Therefore, it seems to be an intrinsic feature of the star, not an artefact introduced by the telluric correction. This vast broadening could be attained by the Stark effect observed in the most intense hydrogen lines, but also by blends with the He I lines. As the lines of He I are quite strong in the spectral type B2-B3, the red broad absorption feature might be contaminated by the He I λ4.056 µm absorption line. Other significant features present in the L band are the remarkable Hu$_{14}$ (H I 6–14) emission line and a conspicuous emission component at the core of He I λ4.038 µm.

To disentangle absorption and emission line components, we built a code using the Python package *LMFit* (Non-Linear Least-Square Minimization and Curve-Fitting for Python, see Newville et al. 2014, 2016) that enables multiple Gaussian profiles to be fit over the spectra (see, e.g. Bosch et al. 2019). This simple procedure also allowed us to determine the line EWs of each component (see Fig. 2). We used the *splot* IRAF tool to measure the rest of the lines. Tables 2 and 3 list the measured line EWs in the K and L bands for all the epochs, respectively.

The errors correspond to values obtained by performing Gaussian fittings. Therefore, larger uncertainties are expected when the Stark effect is the dominant source of broadening. However, Lenorzer et al. (2002) found, from ISO (the Infrared Space Observatory) spectra, that the hydrogen lines of B supergiants do not show a significant spectral type dependence, but they remain roughly constant. In addition, these authors stated that normal B-type stars usually do not exhibit evident Humphreys absorption profiles, so a correction of the EWs is not required.

3.2. Variability in the line EWs

The line profile variability becomes evident in Fig. 3, where we show the Brα, Brγ, and Hu$_{14}$ lines observed at different epochs. The changes in the intensity, and sometimes in the shape of the lines, are noticeable. From the measurements of the line EWs (Tables 2 and 3), we found that the emission and absorption components of Brα display variations of ~40% and ~20% from mean values of 5.15 ± 0.12 Å and 4.99 ± 0.28 Å, respectively. The emission and absorption components of Brγ deviate by 60% and 20% from their corresponding mean EWs of 0.15 ± 0.05 Å and 2.40 ± 0.07 Å. The most variable behaviour is detected in Hu$_{14}$, with line EW variations of more than 70% around a mean value of 0.35 ± 0.03 Å.

Although the H lines could affect the EWs of the nearby He lines, the observed variation in the line EWs is very significant. In the K band, the absorption lines of He I at 2.161 µm, 2.162 µm, and 2.164 µm show variations of 15%, 57%, and 37% concerning a mean value of 0.47 ± 0.03 Å, 0.21 ± 0.02 Å, and 0.43 ± 0.04 Å, respectively. Also the He I line at 4.049 µm has deviations of 20% around 2.36 ± 0.09 Å. The Mg II lines are slightly variable. The measured EW ratio of EW(Mg II 2.137)/EW(Mg II 2.143) ~2 agrees with their line oscillator strength ratio. This value is expected from an optically thin circumstellar envelope.

Figure 4 displays temporal variations in the EWs of H, as well as He lines. The behaviour of the emission lines seems to have a cyclic variation with a period similar to that found by Kraus et al. (2015, 22.5 days). Fittings to the observed variations were done with the Period04 tool (Lenz & Breger 2005), shown in Fig. 5. Periods of 16.0 and 19.9 days are found for the Brα emission. The Brγ absorption feature presents variations with periods of 11.9 and 28.3 days, while the period measured for the Hu$_{14}$ emission is 26.1 days. Periods of 25.6 and 21.6 days are also present in the lines of He I $\lambda\lambda$ 2.162 and 2.181 µm, respectively. Instead, the He I λ 2.164 µm line shows variations of 11.3 days and 49.6 days; this last could be an alias. We could then say that, on average, we found line variations with periods of ~13 and ~23 days. However, a large dispersion of values and alias periods are expected in samples with very few data points.

4. Line fittings

4.1. Atmospheric model and NLTE radiative transfer

To derive the mass-loss rate from line profile fittings, we built an atmospheric model that includes a photosphere and a wind. The layers underlying the photosphere ($\tau_{5000} > 1$) are assumed in hydrostatic equilibrium. To this aim, we adopted the density and temperature structure from the Kurucz models (Kurucz 1979) for the T_{eff} and log g of the star. Above the photosphere, the density distribution and β-law profile are provided by the wind model, considering the mass-loss rate ($\dot{M}$), the terminal velocity (v_{∞}), and the exponent β of the velocity law as free parameters.
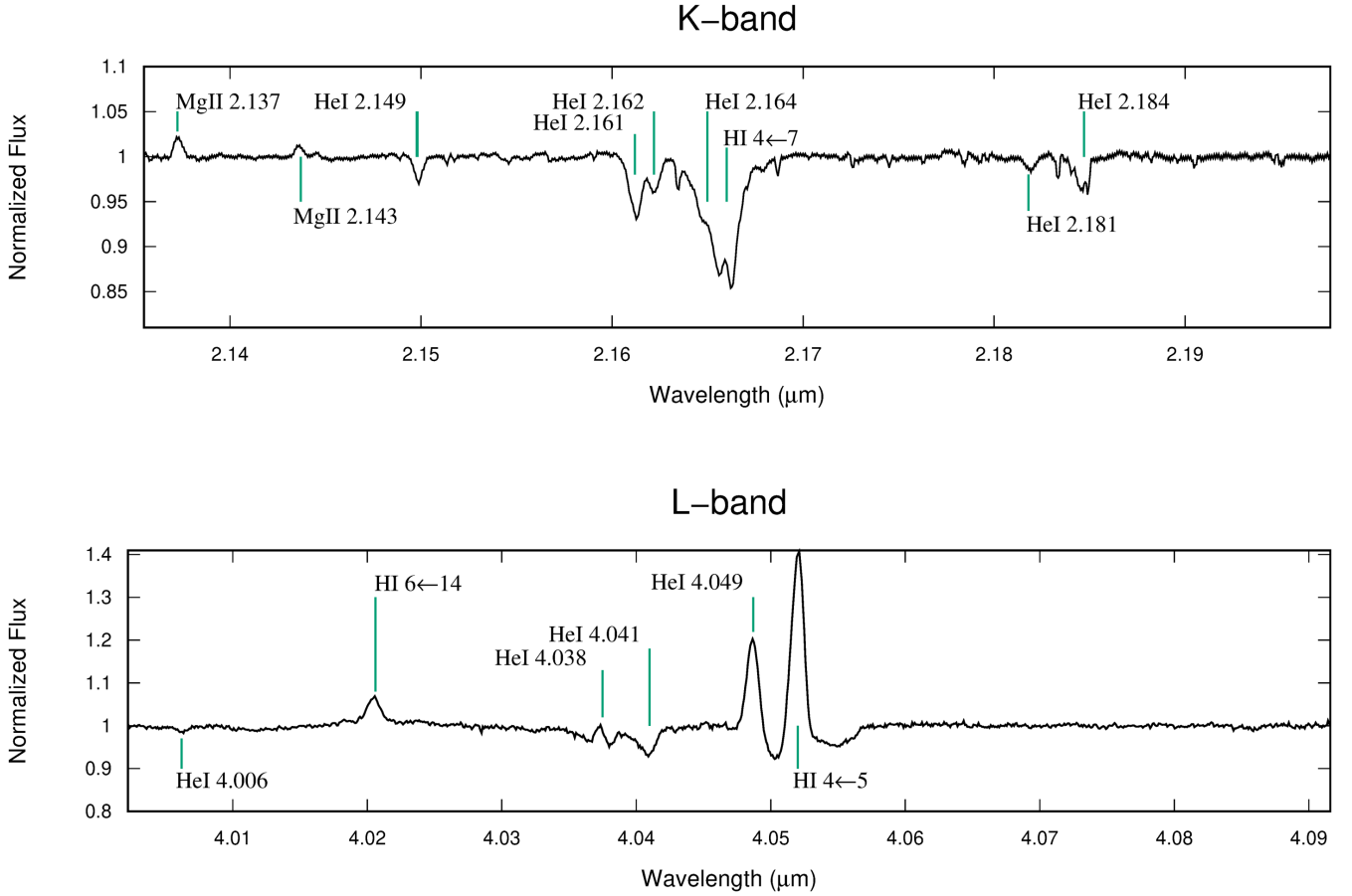
K–band

L–band

Fig. 1. Examples of the *K*- (top) and *L*-band (bottom) spectra of 55 Cyg with the identified lines marked and labelled.

Table 2. EW measurements (in Å) of absorption and emission lines taken in the *K* band.

HJD	Mg II λ2.137	Mg II λ2.143	He I λ2.149	He I λ2.161	He I λ2.162	He I λ2.164	$Br\gamma_{ab}$	$Br\gamma_{em}$	He I λ2.181	He I λ2.184
2457162	−0.09 ± 0.01	−0.04 ± 0.01	0.16 ± 0.02	0.51 ± 0.04	0.24 ± 0.04	0.44 ± 0.04	2.07 ± 0.07	−0.06 ± 0.05	0.10 ± 0.01	0.35 ± 0.03
2457181	−0.08 ± 0.01	—	0.20 ± 0.02	0.50 ± 0.02	0.12 ± 0.02	0.46 ± 0.04	2.51 ± 0.05	−0.15 ± 0.04	0.07 ± 0.01	0.30 ± 0.03
2457187	−0.11 ± 0.01	−0.05 ± 0.01	0.15 ± 0.02	0.52 ± 0.03	0.24 ± 0.03	0.59 ± 0.04	2.88 ± 0.06	−0.06 ± 0.02	0.11 ± 0.01	0.26 ± 0.03
2457193	−0.13 ± 0.01	−0.06 ± 0.01	0.16 ± 0.02	0.41 ± 0.04	0.26 ± 0.04	0.33 ± 0.05	2.28 ± 0.09	−0.11 ± 0.08	0.17 ± 0.01	0.26 ± 0.03
2457195	−0.12 ± 0.01	−0.06 ± 0.01	0.15 ± 0.02	0.51 ± 0.02	0.26 ± 0.02	0.38 ± 0.04	2.53 ± 0.06	−0.22 ± 0.05	0.11 ± 0.01	0.30 ± 0.03
2457198	—	−0.03 ± 0.01	0.13 ± 0.01	0.44 ± 0.05	0.18 ± 0.03	0.49 ± 0.05	2.56 ± 0.07	−0.24 ± 0.04	0.10 ± 0.01	0.20 ± 0.02
2457202	—	−0.04 ± 0.01	0.14 ± 0.01	0.47 ± 0.01	0.16 ± 0.01	0.43 ± 0.04	2.38 ± 0.06	−0.23 ± 0.07	0.07 ± 0.01	0.20 ± 0.02
2457203	−0.13 ± 0.01	−0.05 ± 0.01	0.15 ± 0.02	0.40 ± 0.02	0.19 ± 0.02	0.33 ± 0.03	1.97 ± 0.06	−0.30 ± 0.06	0.09 ± 0.01	0.23 ± 0.02

Notes. Negative values are for emission line components, and dashes indicate the absence of the line.

Table 3. EW measurements (in Å) of absorption and emission lines taken in the *L* band.

HJD	He I λ4.006	Hu_{14}	He I λ4.041	He I λ4.049	$Br\alpha_{ab}$	$Br\alpha_{em}$
2456591	0.16 ± 0.02	−0.41 ± 0.02	0.86 ± 0.09	−1.98 ± 0.07	4.75 ± 0.19	−2.83 ± 0.06
2457162	0.20 ± 0.04	−0.19 ± 0.05	0.75 ± 0.07	−2.43 ± 0.08	4.05 ± 0.20	−6.64 ± 0.10
2457181	0.31 ± 0.03	−0.07 ± 0.01	0.98 ± 0.09	−1.94 ± 0.08	5.15 ± 0.23	−5.03 ± 0.17
2457187	0.12 ± 0.01	−0.06 ± 0.01	0.95 ± 0.09	−2.15 ± 0.08	4.58 ± 0.22	−4.60 ± 0.10
2457193	−	−0.53 ± 0.06	0.70 ± 0.10	−2.50 ± 0.22	5.39 ± 0.69	−6.41 ± 0.31
2457195	0.12 ± 0.01	−0.55 ± 0.05	0.80 ± 0.08	−2.74 ± 0.07	5.09 ± 0.25	−5.80 ± 0.08
2457202	0.11 ± 0.01	−0.36 ± 0.01	1.05 ± 0.10	−2.29 ± 0.05	5.35 ± 0.14	−4.86 ± 0.07
2457203	0.23 ± 0.04	−0.62 ± 0.03	1.24 ± 0.10	−2.84 ± 0.10	5.54 ± 0.33	−5.05 ± 0.09

Notes. Negative values are for emission line components, and dashes indicate the absence of the line.
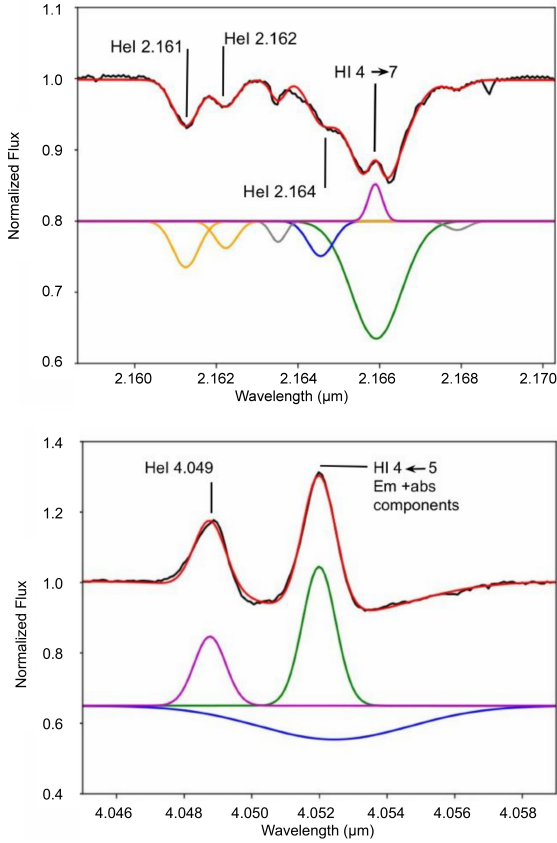
Fig. 2. Gaussian fittings to the observed Brγ (H I 4–7, top panel) and Brα (H I 4–5, bottom panel) line profiles that disentangle emission and absorption components. The spectra shown here were taken on June 22 and June 28, 2015, respectively. The fittings combining all contributing Gaussian components (solid red line) are overlaid on the observations in black. The individual Gaussian components used to model the lines are shown with different colours and have been shifted down in the y direction for better visualisation.

A Kurucz model represents the temperature distribution across the photosphere. The wind temperature law is input data, given as a piecewise linear function of the radial distance from the star's centre. Some examples are the temperature structure from flux-weighted mean opacities in a spherical and diluted envelope (Sundqvist et al. 2019; Gormaz-Matamala et al. 2022) or an isothermal wind temperature law. In the particular case of this research, we used the same velocity and temperature structure obtained in Kraus et al. (2015).

A smooth transition is considered between the density structure of the photosphere and the wind using the mass continuum equation. The final set of wind parameters ($\dot{M}$, v_∞, and β) is the one that achieves the best fitting between synthetic and observed line profiles.

To compute the hydrogen lines, we used the APPEL code (Mihalas & Kunasz 1978; Catala & Kunasz 1987) that solves the equations of radiative transfer and statistical equilibrium for level populations consistently; then, it computes the emergent flux profiles in the direction of the observer. The code APPEL treats a non-local thermodynamic equilibrium (NLTE) multi-level-atom problem in the fluid co-moving frame along a set of given parallel rays (the conventional p-z geometry; see Fig. 1 in Catala & Kunasz 1987) for a spherically symmetric monotonic expanding outflow. The code uses the ETLA method (equivalent two-level atom approach) as developed for stellar winds by
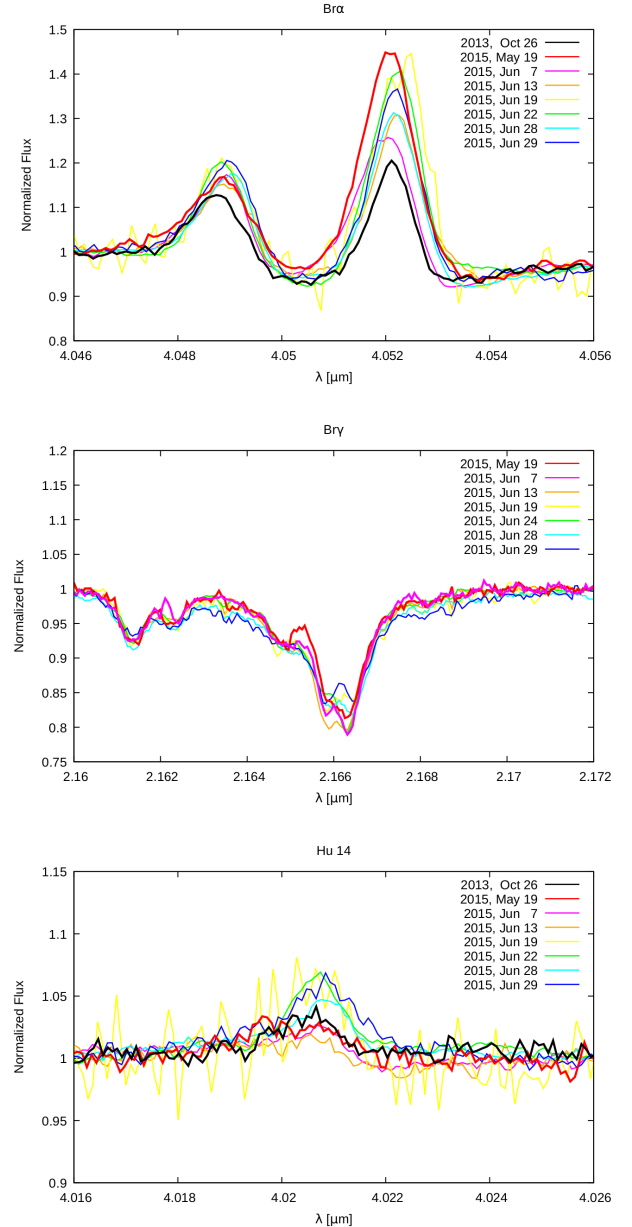

Fig. 3. Variability observed in the Brα (top panel), Brγ (middle panel), and Hu$_{14}$ (bottom panel) line profiles on different dates. A different line thickness was used to visualise line profile changes for the first two dates.

Mihalas & Kunasz (1978). It performs an iterative cycle that does the following: i) solves the radiative transfer for each line and continuum, isolated from the multi-level atomic context; and ii) uses the level populations determined by solving the set of simultaneous rate equations. It uses an acceleration method developed by Ng (1974) to improve the rate of convergence (see details in Catala & Kunasz 1987, Sect. 4). The iterative cycle is performed until convergence of the occupation numbers of atoms is achieved. Generally, around five to seven iterations are needed.

The emergent line profiles are then calculated by solving the radiative transfer equations in the observer's frame on the defined set of parallel rays. To represent the line profile function, a Doppler profile is adopted, and its half-width is determined by V_{th} (the mean Doppler random velocity) and V_{micro} (the microturbulent speed). To calculate the continuum radiation, we evaluated background opacity and emission sources in LTE,
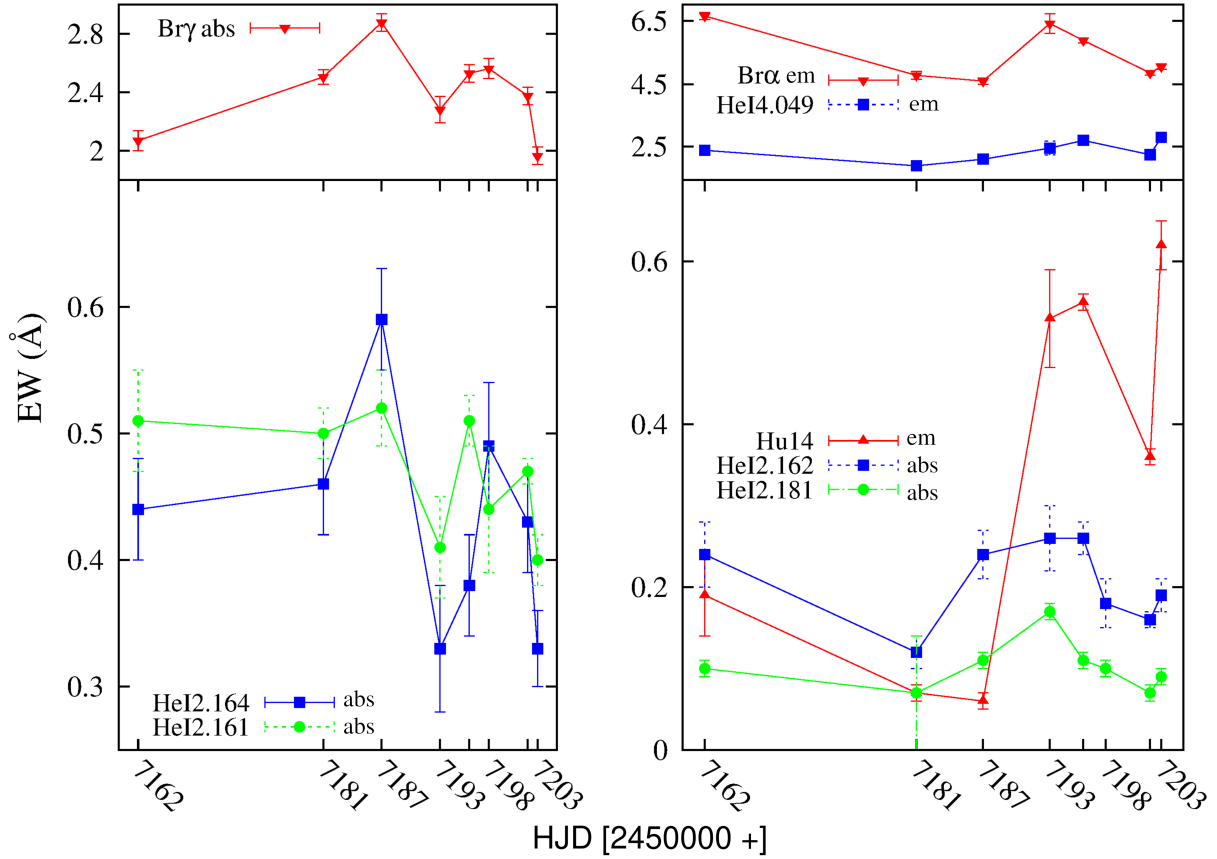
Fig. 4. Line EW variations of H and He lines present in the *K* and *L* bands. Left panel: EWs of absorption lines. Right panel: EWs of emission lines (absolute values), except for the lines of He I that are in absorption. The variation of the emission component of Brα is displayed in the upper right panel.

considering a dilution factor and the radiation and electron temperatures, as described by Mihalas (1978, Eqs. (5)–(46)). As background sources, the model includes ten levels for He I, 20 levels for He II and He III, and a total of 24 levels for C, N, Ne, O, Si, and their corresponding ions. Radiative and collisional ionisation cross sections for hydrogen are from Mihalas (1967), and collisional excitation cross sections are given by Klein & Castor (1978). The density, opacity, and velocity distributions are specified on the grid points. The grid is used without refinement to solve the radiative transfer in the co-moving frame.

We improved the code APPEL to treat an H atom plus continuum with 23 levels in NLTE instead of the six-level atom considered in its original version (Catala & Kunasz 1987; Cidale & Ringuelet 1993). This allowed us to calculate the NIR H lines.

4.2. Comparison with observations

As the T_{eff} and log g values derived from both optical and IR data are usually in good agreement (Repolust et al. 2005), we adopted atmospheric models with T_{eff} between 18 000 K and 20 000 K, and log g = 2.5 dex. These parameters are close to the mean values (T_{eff} = 18 600 K and log g = 2.4 dex) used by Kraus et al. (2015) for 55 Cyg to analyse its optical spectrum. We also adopted from that work the stellar radius, $R_\star$, in the interval 57–62 $R_\odot$, the projected rotation speed, $V \sin i \sim 40$–45 km s^{-1}, and the micro and macroturbulence velocities, V_{micro} and V_{macro}, respectively. The selected values for T_{eff} and $R_\star$ are also in good agreement with those calculated by Gordon et al.

(2019, T_{eff} = 18 800 K, and $R_\star$ = 56.7 $R_\odot$) using interferometric techniques.

To test the result of the 23-level H atom computed with the APPEL code, we calculated the Hα line for the observation taken on October 26, 2013, and used the same wind structure reported in Kraus et al. (2015). This observation was selected because it was taken on the same night as one of our NIR spectra. The emergent synthetic line profile was convolved with a rotational broadening function using the projected rotation velocity of the star. The line broadening due to the instrumental function was also taken into account by adopting a Gaussian kernel function.

The best fitted model, shown in Fig. 6, was obtained for T_{eff} = 20 000 K and log g = 2.5 dex, which is in excellent agreement with the observed Hα line and the fitting done in Kraus et al. (2015, for the same observation). We found a massloss rate discrepancy of 10% between that work ($\dot{M}$ = 1.8 × 10^{-7} $M_\odot$ yr^{-1}) and the result from the APPEL code ($\dot{M}$ = 2 × 10^{-7} $M_\odot$ yr^{-1}). The same wind model also reproduces the Brα emission line well with an agreement within 10%, as shown in Fig. 7. For a discussion on the chosen parameters, readers can refer to Sect. 5.2. The broadening effect due to the macroturbulence is also shown as an example in the models. Its increment partly compensates for the wide broadening of the absorption component but also affects the emission line, which exhibits full widths at half maximum (FWHM) between 71.4 km s^{-1} (October 26, 2013) and 89.5 km s^{-1} (June 7, 2015), with a mean value of 82.2 km s^{-1}. Furthermore, as we do not include Stark broadening, the total width of the broad photospheric component
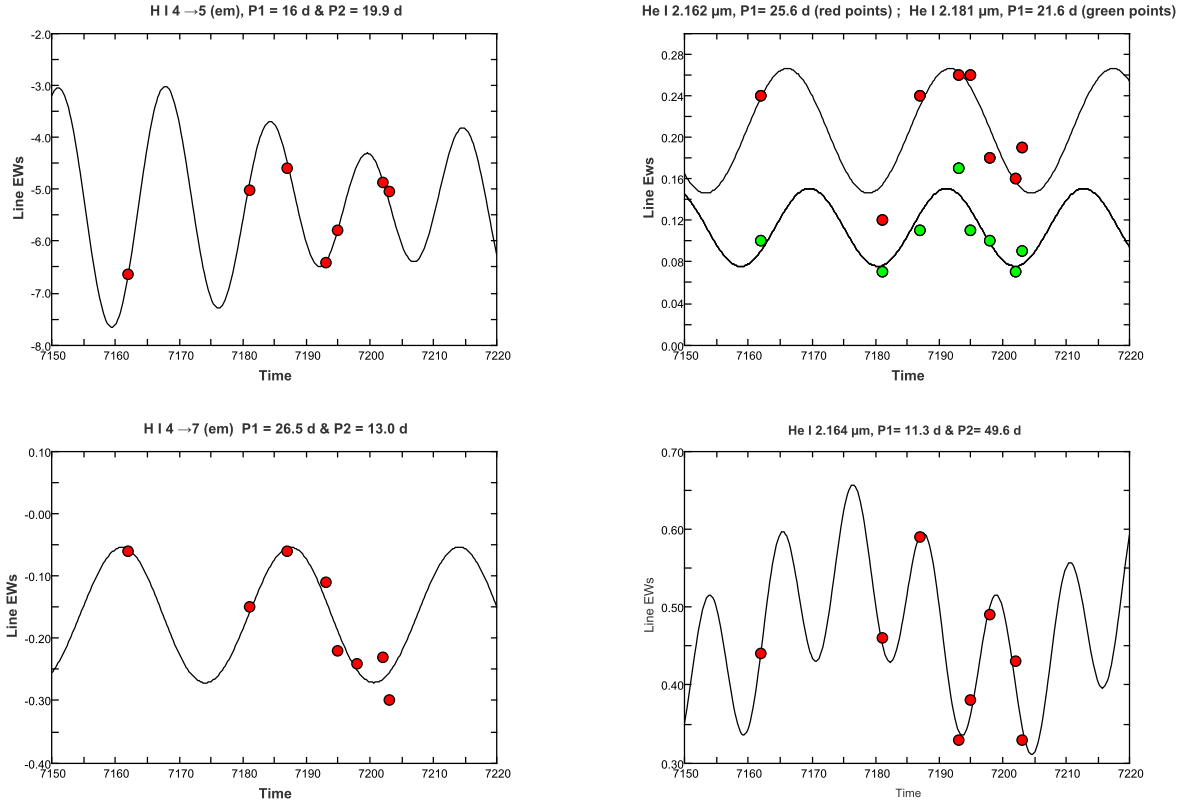
Fig. 5. Examples of time-series fittings to the line EW variations of H (left panels) and He (right panels) lines. The line EWs and time are in Å and HJD-2450000 days, respectively.
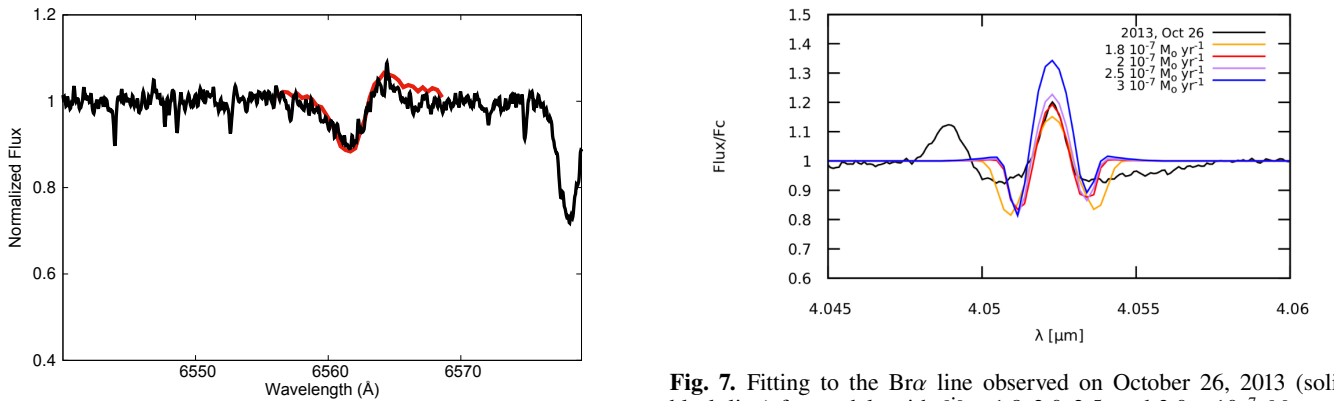

Fig. 6. Fitting to the Hα profile observed in 2013 (solid red line) obtained with $\dot{M} = 2 \times 10^{-7}\ M_\odot\ \text{yr}^{-1}$.

Fig. 7. Fitting to the Brα line observed on October 26, 2013 (solid black line) for models with $\dot{M} = 1.8, 2.0, 2.5$, and $3.0 \times 10^{-7}\ M_\odot\ \text{yr}^{-1}$. The best-fitting model to the observation taken in 2013 is for $\dot{M} = 2 \times 10^{-7}\ M_\odot\ \text{yr}^{-1}$ and $V_{\text{macro}} = 25\ \text{km s}^{-1}$. The model for $\dot{M} = 1.8 \times 10^{-7}\ M_\odot\ \text{yr}^{-1}$ was calculated with $V_{\text{macro}} = 30\ \text{km s}^{-1}$ to show the broadening. The observed emission component has an FWHM value of $71.4\ \text{km s}^{-1}$.

is not reproduced. Nevertheless, the extended red wing might also be contaminated by He I lines (see Sect. 3.1).

As the Brα line is highly variable, it is not easy to describe its behaviour with a unique set of wind parameters; therefore, we had to model it with different mass-loss rates and macroturbulence velocities. Although a high value of $\dot{M} = 9 \times 10^{-7}\ M_\odot\ \text{yr}^{-1}$ can reproduce the most intense Brα line observed, it also predicts a P Cygni profile for Hu$_{14}$, a morphology that was not observed during that epoch (see details below in Sect. 5.1). Therefore, we had to model the observed spectra within a restricted interval in the mass loss. Best-line fittings to all the NIR spectra were obtained for models with $T_{\text{eff}} = 20\,000$ K and $R_\star = 57\ R_\odot$ and with $\dot{M}$ between $2\ 10^{-7}$ and $7\ 10^{-7}\ M_\odot\ \text{yr}^{-1}$. These fittings are shown in Fig. 8. The fittings were done by eye, checking that

the synthetic line profiles would reasonably match the variations seen in Brα and Hu$_{14}$ lines. The corresponding model parameters are given in Table 4 and show changes in the mass-loss rate by a factor of 3.5 between 2013 and 2015, and up to 2.3 in a short-term period.

We want to emphasise that not only did we observe mass-loss changes within a few weeks, but also the emission lines displayed different broadening. Thus, to match their slight variations well, little changes in V_{mac} (between 25 km s^{-1} and 30 km s^{-1}) were needed. Evidence of line-profile variability connected with a macroturbulent broadening in OB supergiants was
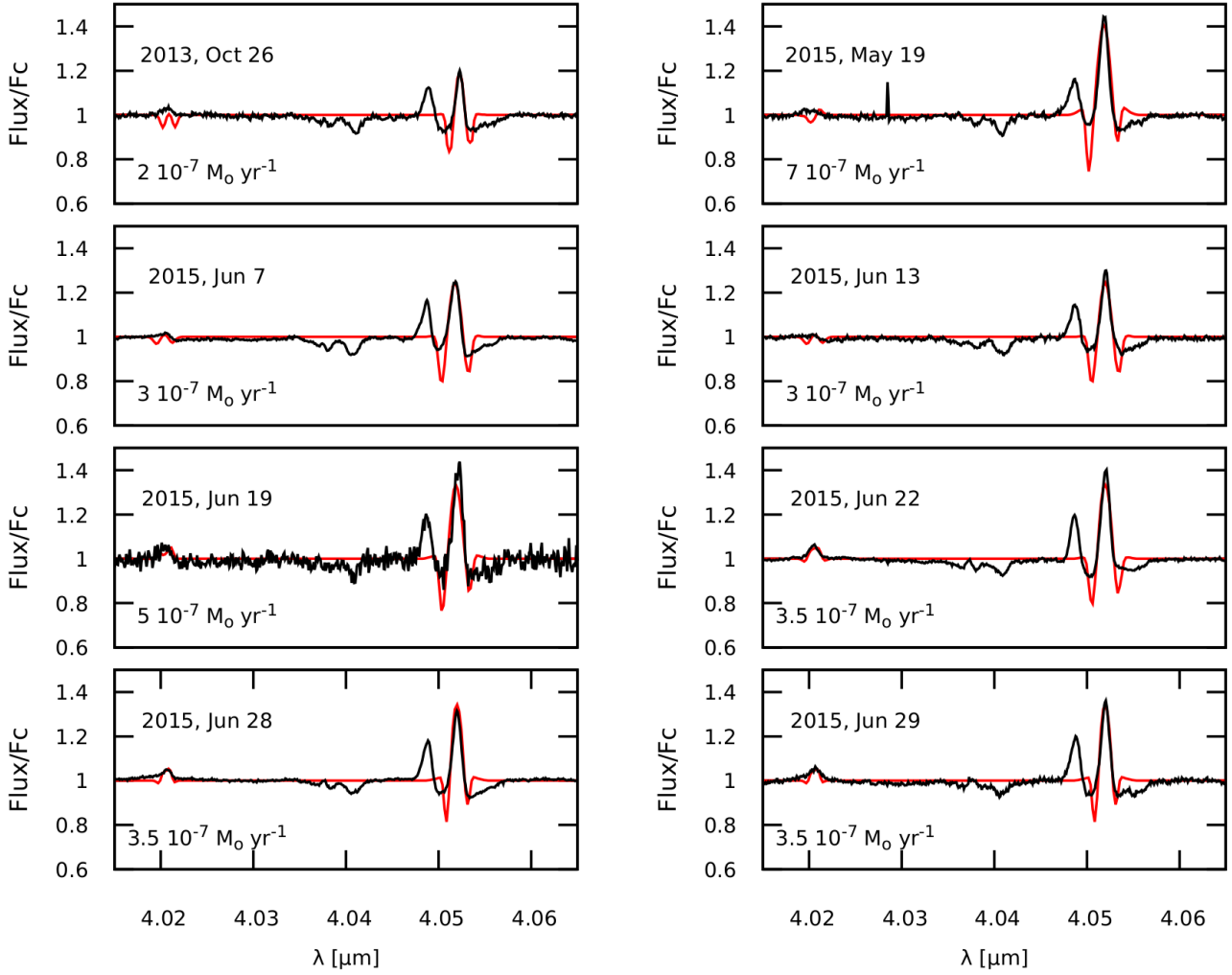
Fig. 8. Best-fitting models to the Brα and Hu$_{14}$ emission observed in 2013 and 2015. Observations are traced in black, and models are in solid red lines. The mass-loss rate used to model the lines is indicated in each plot.

Table 4. Wind model parameters for NIR observations.

Date (dd-mm-yy)	$T_{\rm eff}$ (K)	$R_\star$ ($R_\odot$)	β	$\dot{M}$ [10^{-6}] $M_\odot$ yr^{-1}	V_∞ (km s^{-1})	$V_{\rm mic}$ (km s^{-1})	$V_{\rm macro}$ [km s^{-1}]
26-10-13	20 000	57	2	0.20	270	15	25
19-05-15	20 000	57	2	0.70	270	15	30
07-06-15	20 000	57	2	0.30	270	15	30
13-06-15	20 000	57	2	0.30	270	15	30
19-06-15	20 000	57	2	0.50	270	15	30
22-06-15	20 000	57	2	0.35	270	15	30
28-06-15	20 000	57	2	0.35	270	15	25
29-06-15	20 000	57	2	0.35	270	15	25

Notes. A variation in $\dot{M}$ by a factor of ~2 is present within a three-week time interval. The mass-loss rates correspond to unclumped wind models.

reported by Simón-Díaz et al. (2010), and this phenomenon was related to stellar oscillations.

5. Discussion

We have presented NIR spectra of the BSG star 55 Cyg that provide observational evidence of mid-term variability in the

photosphere and the wind with periods of ~13 and 23 days. This result agrees with the period of 22.5 days found by Kraus et al. (2015). Furthermore, using the code APPEL, we modelled the Brα and Hu$_{14}$ lines for the epochs of observations. We also obtained a consistent result when modelling the Hα line observed in 2013 and the NIR lines with a mass-loss rate of 2×10^{-7} $M_\odot$ yr^{-1}. This value agrees with the mean mass-loss rate also derived by Kraus et al. (2015) from Hα. However, we found that the mean mass-loss rate derived from the spectra taken in 2015 is almost twice the value obtained in 2013. Furthermore, such a variation in the mass loss was also detected on a much shorter timescale (within three weeks; see Table 4), supporting the hypothesis of strange-mode instability. The occurrence of strange-mode pulsations in 55 Cyg is extensively discussed by Kraus et al. (2015) and Yadav & Glatzel (2016). Moreover, this phenomenon could produce mass-loss amounts from the star similar to that provided by the line-driven wind theory.

5.1. NIR lines to diagnose mass-loss rates

We study the formation of NIR H recombination lines from radiative transfer models, assuming they form in a homogeneous radiatively driven wind. We find a generally good agreement in the profile morphology and line strength between the model and
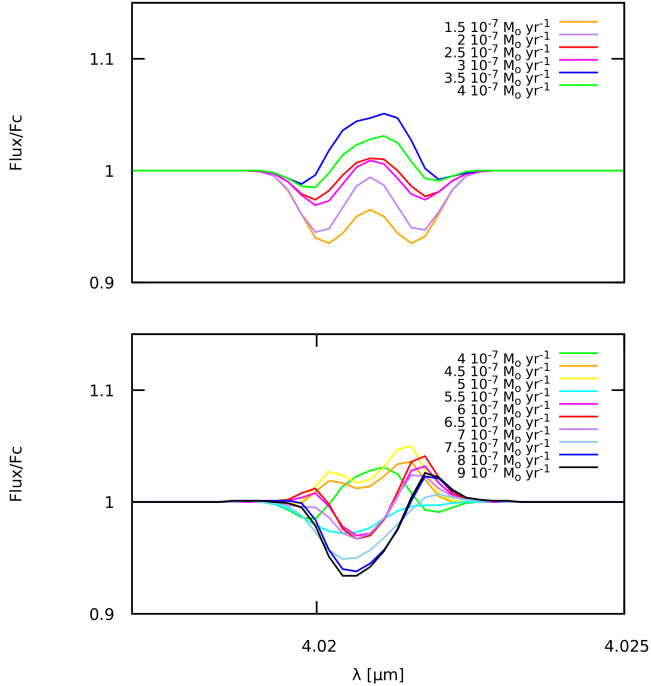
Fig. 9. Response of the line Hu_{14} to the mass-loss rate. Top panel: As the mass-loss increases, the line changes from an absorption profile to a single-peaked emission. The mass-loss interval goes from $1.5 \times 10^{-7}\ M_\odot\ yr^{-1}$ to $4 \times 10^{-7}\ M_\odot\ yr^{-1}$, in a step of $0.5 \times 10^{-7}\ M_\odot\ yr^{-1}$. The maximum intensity of the single-peaked emission is achieved when $\dot{M} = 3.5 \times 10^{-7}\ M_\odot\ yr^{-1}$ (solid blue line), and then the intensity decreases (solid green line). Bottom panel: Synthetic double-peaked-profiles were obtained from $4.5 \times 10^{-7}\ M_\odot\ yr^{-1}$ to $7 \times 10^{-7}\ M_\odot\ yr^{-1}$. The behaviour is non-monotonic. Then, as the mass loss increases, the profile turns to a P Cygni one (for $\dot{M} > 7.5 \times 10^{-7}\ M_\odot\ yr^{-1}$).
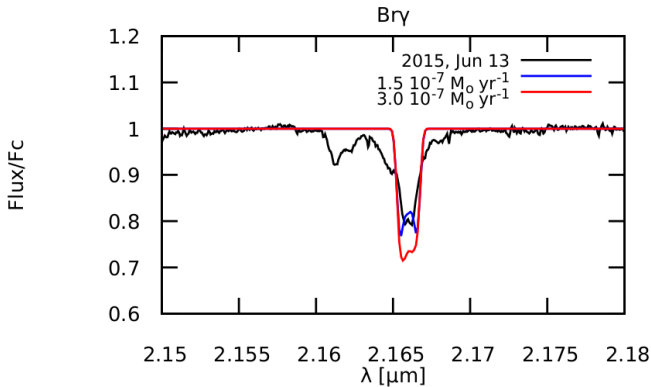
Fig. 10. Fittings to the $Br\gamma$ line profile. When the mass loss increases, the synthetic line profile becomes deeper. The best fitting is obtained with a lower mass-loss rate ($\dot{M} = 1.5 \times 10^{-7}\ M_\odot\ yr^{-1}$). The line is blended with He I $\lambda 2.184$ μm. Readers can refer to the main text for details.

the observations (see Fig. 8). As our model represents a homogeneous wind, we provide values of unclumped mass-loss rates. However, even though clumpiness might be weaker compared to O stars in the BSG domain (cf. Driessen et al. 2019), it could still lead to an overestimation of the mass-loss rate when it is neglected. The mass-loss rate would decrease by a factor $1/\sqrt{f_{cl}}$ if the so-called clumping factor, f_{cl}, is assumed constant (this assumption is unlikely for dense winds; see e.g. Puls et al. 2006; Najarro et al. 2011). Therefore, the mass-loss rates obtained in

this work might be considered upper limits, but their variability should be preserved if the clumping factor is constant.

It is also interesting to remark that the emission line Hu_{14} is sensitive to mass loss but it might present a non-monotonic behaviour. This line puts constraints on the mass-loss upper limit. As an example, Fig. 9 shows the behaviour of Hu_{14} when changing the mass loss in almost an order of magnitude. Increasing the mass-loss rate, the shape of the Hu_{14} line turns from an absorption line (not shown) to single-peak emission (upper panel). Its intensity increases monotonically when varying $\dot{M}$ from $1.5 \times 10^{-7}\ M_\odot\ yr^{-1}$ to $3.5 \times 10^{-7}\ M_\odot\ yr^{-1}$. Then, for $\dot{M} = 4 \times 10^{-7}\ M_\odot\ yr^{-1}$, the intensity decreases (shown with a solid green line). The bottom panel of the figure displays a double-peaked profile for mass-loss rates between $4.5 \times 10^{-7}\ M_\odot\ yr^{-1}$ and $5.0 \times 10^{-7}\ M_\odot\ yr^{-1}$ and, then, it turns to a P Cygni profile which is very similar for $\dot{M} > 7 \times 10^{-7}\ M_\odot\ yr^{-1}$ (solid black lines). The maximum emission in Hu_{14} was obtained at $3.5 \times 10^{-7}\ M_\odot\ yr^{-1}$ for the selected stellar and wind models.

Concerning the $Br\gamma$ line, which is also blended with He I, all the models predict an absorption line profile with little emission at the core. Nevertheless, as we used a Gaussian profile, the synthetic line profile is deeper at the core and narrower at the wings. Figure 10 shows the observation taken in June 13, 2015, together with the model used to reproduce the $Br\alpha$ line ($\dot{M} = 3.0 \times 10^{-7}\ M_\odot\ yr^{-1}$). However, a model with a lower $\dot{M} = 1.5 \times 10^{-7}\ M_\odot\ yr^{-1}$ would fit the observed feature better. In increasing the mass-loss rate, the synthetic absorption feature becomes deeper, while the observed line decreases in intensity.

The discrepancies between the synthetic and observed $Br\gamma$ and Hu_{14} lines could be related to our simple ionisation model, which does not account for line-blocking effects or the adopted line profile. Moreover, the ionisation model could also influence the atom-level population leading to the non-linear behaviour of Hu_{14} lines. The observations show this line only in emission, while the synthetic spectra sometimes yield different predictions. The influence of NLTE departure coefficients for the lower and upper levels of lines formed in the IR is discussed in detail by Najarro et al. (2011).

On the other hand, based on the results of the 'unclumped' mass-loss rate given in Table 4 and the EW of the $Br\alpha$ emission component (listed in Table 3), we derived the following linear regression, plotted in Fig. 11 with a solid blue line:

$$\log \dot{M} = 0.98(\pm 0.25) \log(-EW_{Br\alpha\,(em)}) - 7.13(\pm 0.18). \quad (1)$$

The linear fitting to our data (blue symbols) is compared with that derived by Lenorzer et al. (2002, solid red line). These authors' samples consist of O-type stars and B-type supergiants (red squares) with mass-loss rates obtained from either $H\alpha$ or radio measurements. Some of those observations match our linear relation. The difference could be due to several factors, that is, the characteristic star sample (O-type and B-type supergiants) measured on low-resolution spectra, the use of different wind models for deriving mass-loss rates, or the fact that we used a restrictive parameter range. Since our relationship was obtained from observations of the same variable star, it could only apply to describe the mass-loss variations of other B supergiants with a similar range of parameters.

Here, we have assumed that line intensity variations of the $Br\alpha$ emission component (within a short time interval of 22.5 days) can be attributed to changes in mass loss; the larger the mass-loss rate, the more intense the line emission, as shown in Fig. 11. However, it is difficult to assert if these line intensity variations are only produced by changes in the mass-loss rates
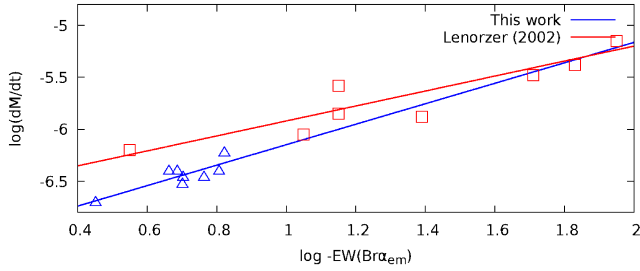
Fig. 11. Measured Brα EWs vs. the mass-loss rates of 55 Cyg at different epochs (blue symbols). The linear correlation (blue line) to our data is compared with the relationship found by Lenorzer et al. (2002), which was obtained from ISO spectra of O-type stars and B-type supergiants (red line and square symbols) where the mass-loss rate was obtained from Hα or radio measurements.

because an increment in the line intensity could also occur if $R_\star$ (or V_∞) decreases, keeping $\dot{M}$ constant.

5.2. Uncertainties as to the mass-loss rates

In this section, we explore the uncertainties as to the mass-loss rate due to the adopted $T_{\rm eff}$ value, particularly because 55 Cyg shows $T_{\rm eff}$ variations between 18 600 K and 19 100 K (Kraus et al. 2015). Therefore, we computed models with $T_{\rm eff} = 18\,000$ K and $T_{\rm eff} = 20\,000$ K, but using the same wind temperature law based on the selected model for the Hα line. Figure 12 illustrates a comparison of the intensity of the Brα line using the lower and upper $T_{\rm eff}$ limits for a given range of $\dot{M}$. A model with a $T_{\rm eff} = 18\,000$ K produces a less intense line profile for the same mass-loss rate. Therefore, the mass loss must be increased from 2×10^{-7} $M_\odot$ yr^{-1} to 2.5×10^{-7} $M_\odot$ yr^{-1} to recover a good fitting. This result seems to be in apparent contradiction with the scaling property related to the impact of the ionisation and excitation, approximated by $Q \propto \dot{M}/T_{\rm eff}$ (the lower $T_{\rm eff}$, the lower $\dot{M}$ for a given EW; e.g. Lenorzer et al. 2002). However, as we kept $T_{\rm wind}$ constant, the intensities of the recombination lines scale with the radiative recombination rate ($R_{ki} \propto N_{\rm e}\ T_{\rm wind}^{-1/2}$), so the local electron density ($N_{\rm e}$) changes because of $T_{\rm eff}$.

On the other hand, the discrepancy that results from adopting $T_{\rm eff} = 20\,000$ K instead of the mean value derived by Kraus et al. (2015, 18 600 K) could also be attained by our simple ionisation model (see Sects. 4.1 and 5.1) that leads to a decrease in the pseudo-continuum (see Fig. 9 in Puls et al. 2008).

Optical and IR spectral variations reported by Kraus et al. (2015) and this work indicate that the effective temperature of 55 Cyg is almost constant ($\Delta\,T_{\rm eff} \sim \pm 1000$ K). However, the stellar radius might vary with an amplitude of about 10% ($\Delta\,R_\star \sim 6\,R_\odot$), leading to similar results for $\dot{M}$ variations. Variations in $\Delta R_\star$ are expected from non-adiabatic radial pulsations, where extensive changes in the stellar radius of 15–30% (depending on the mass of the star) would take place at almost a constant $T_{\rm eff}$ (Yadav & Glatzel 2016).

5.3. Formation of rings or shell structures

The detection of the IR Mg II doublets in emission is not a common property among classical B supergiants (Hanson et al. 1996). This doublet is likely excited via Ly fluorescence (Bowen 1947). Emission lines of Mg II are only seen in stars with spectral types earlier than B4, usually in extreme emission line objects, such as B[e] and LBV stars (Lenorzer et al. 2002; Oksala et al. 2013; Cochetti et al. 2020). However, these features have also been reported in one peculiar B2 Ia star (Morris et al. 1996) and
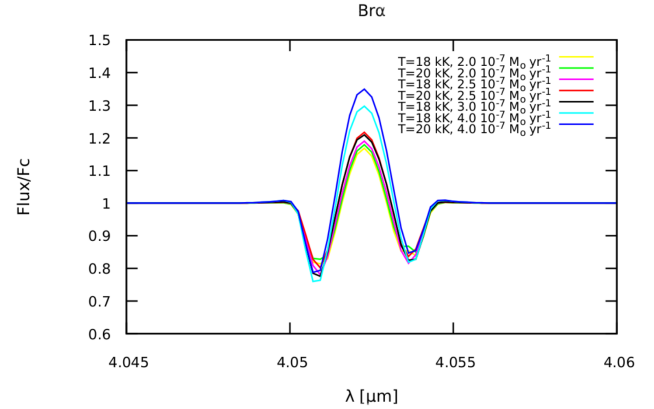
Fig. 12. Response of the fittings to $T_{\rm eff}$. A lowering in temperature of 2 000 K might need an increment in $\Delta\dot{M} = 0.5 \times 10^{-7}$ $M_\odot$ yr^{-1} to reproduce the line intensity, such as is the case of models in red and black solid lines.

some Be early-type stars (Clark & Steele 2000). Therefore, the appearance of these emission lines seems to point to the existence of circumstellar rings or shells, similar to what is seen in Sher 25 or SN 1987A. In this respect, it is worth mentioning that radial pulsations have also been detected in the LBV candidate Sher 25 (Taylor et al. 2014) and Lovekin & Guzik (2014) suggest that pulsations could be the origin of S Dor outbursts, which are often connected with a phase of enhanced mass loss and mass ejections, which may lead to the formation of persistent circumstellar gas rings.

On the other hand, if radial strange mode instabilities are present, they might go along with strong shock waves running through the atmosphere, since the heat transfer by an oscillating flow leads to variations in the temperature at the base of the wind. This phenomenon might also account for the emission line of He I at $\lambda 4.049$ μm. This line has only been observed in pure emission in many B1-B2 stars, mainly in β Cepheid variables (Zaal et al. 2001, 1999, 1997). Zaal et al. (1999) suggested that this line originates in the photosphere, but there should be a different mechanism that heats the He I forming region so that the degree of ionisation of that region is higher than in the deeper atmosphere.

5.4. The evolutionary state of 55 Cyg

Regular low-amplitude radial pulsations in massive stars were encountered during the core hydrogen burning as well as during the early core helium burning stage of evolution (Dorfi & Gautschy 2000). Therefore, the high number of multi-periodic pulsations, detected in 55 Cyg by Kraus et al. (2015), and the bow-shock structure seen in the WISE images are more consistent with the expected characteristic of massive stars evolving back to the blue (Saio et al. 2013). A bow-shock structure could originate from either a wind-ISM interaction that occurred during an RSG phase (Cox et al. 2011) or a wind-wind interaction in a post-RSG phase. Furthermore, it is known that the interaction of a fast, low-density wind that expands into a slow, dense flow that originated by a previous red giant or super-giant phase might also lead to the formation of equatorial rings, shells, or bi-polar structures, similar to the patterns observed around the BSG Sher 25 or SN 1987A.

Based on the aforementioned comments, we believe that 55 Cyg has undergone periods of weak outbursts characterised by enhanced mass-loss rates. If the star were in a post-RSG evolution, this scenario would favour the interaction of its current

fast yet variable wind with the previous slow wind. Therefore, it is highly probable that the star would have developed a circumstellar shell or rings produced by accumulated or compressed circumstellar gas around the star. In this scenario, the star could be transiting the phase of B supergiants with rings (similar to Sher 25) or a pre-S Dor-type LBVs.

6. Conclusions

From the NIR spectroscopic behaviour of 55 Cyg, we found that the mass-loss rate doubled its value between 2013 and 2015. We also detected variations in the EWs of the NIR lines with periods of ∼13 and ∼23 days. Our findings suggest that the variability observed in the star seems to be caused by oscillations with the 22.5-day cycle found by Kraus et al. (2015) and likely its first harmonic. The most plausible explanation is the presence of strange radial modes, as previously suggested by Kraus et al. (2015) and Yadav & Glatzel (2016). These radial pulsations might lead to the propagation of compression density waves with cycles of density enhancements and rarefactions.

In addition, the appearance of emission in the NIR Mg II lines points to the presence of a ring of accumulated or compressed circumstellar gas around the star. This scenario together with the presence of a multi-periodic pulsation and the bow-shock structure seen in the WISE images (Kraus et al. 2015) support a post-RSG evolutionary phase. We propose that 55 Cyg might be either in a pre-LBV phase or a BSG star with rings. Based on the pattern seen around Sher 25 that resembles the triple-ring structure around SN 1987A, we cannot rule out that 55 Cyg as a moderately massive blue supergiant could be a direct progenitor of type II supernovae (Arnett 1989).

It is worth noting the importance of comprehensively monitoring NIR variability in BSGs. This will help to understand the physical properties of their stellar winds in detail and their connection to strange-pulsation modes or resolve new binary systems. In addition, a follow-up and monitoring programme of B supergiants would also help to test the $Br_\alpha - \dot{M}$ relationship of other variable B supergiants.

References

Abbott, D. C. 1982, ApJ, 259, 282
Aerts, C., Lefever, K., Baglin, A., et al. 2010, A&A, 513, L11
Arnett, D. 1989, ApJ, 343, 834
Barlow, M. J., & Cohen, M. 1977, ApJ, 213, 737
Bosch, G., Hägele, G. F., Amorín, R., et al. 2019, MNRAS, 2153
Bowen, I. S. 1947, PASP, 59, 196
Castor, J. I., Abbott, D. C., & Klein, R. I. 1975, ApJ, 195, 157
Catala, C., & Kunasz, P. B. 1987, A&A, 174, 158
Chesneau, O., Dessart, L., Mourard, D., et al. 2010, A&A, 521, A5
Chiosi, C., & Maeder, A. 1986, ARA&A, 24, 329
Cidale, L. S., & Ringuelet, A. E. 1993, ApJ, 411, 874

Clark, J. S., & Steele, I. A. 2000, A&AS, 141, 65
Clark, J. S., Ritchie, B. W., & Negueruela, I. 2010, A&A, 514, A87
Cochetti, Y. R., Kraus, M., Arias, M. L., et al. 2020, AJ, 160, 166
Cox, N. L. J., García-Hernández, D. A., García-Lario, P., & Manchado, A. 2011, AJ, 141, 111
Curé, M., Cidale, L., & Granada, A. 2011, ApJ, 737, 18
De Loore, C., De Greve, J. P., & Lamers, H. J. G. L. M. 1977, A&A, 61, 251
Dorfi, E. A., & Gautschy, A. 2000, ApJ, 545, 982
Driessen, F. A., Sundqvist, J. O., & Kee, N. D. 2019, A&A, 631, A172
Ekström, S., Georgy, C., Eggenberger, P., et al. 2012, A&A, 537, A146
Eldridge, J. J., & Tout, C. A. 2004, MNRAS, 353, 87
Elias, J. H., Rodgers, B., Joyce, R. R., et al. 2006, Proc SPIE, 6269, 626914
Friend, D. B., & Abbott, D. C. 1986, ApJ, 311, 701
Georgy, C. 2012, A&A, 538, A8
Georgy, C., Ekström, S., Meynet, G., et al. 2012, A&A, 542, A29
Glatzel, W., Kiriakidis, M., Chernigovskij, S., & Fricke, K. J. 1999, MNRAS, 303, 116
Gordon, K. D., Gies, D. R., Schaefer, G. H., Huber, D., & Ireland, M. 2019, ApJ, 873, 91
Gormaz-Matamala, A. C., Curé, M., Lobel, A., et al. 2022, A&A, 661, A51
Hanson, M. M., Conti, P. S., & Rieke, M. J. 1996, ApJS, 107, 281
Hanson, M. M., Kudritzki, R. P., Kenworthy, M. A., Puls, J., & Tokunaga, A. T. 2005, ApJS, 161, 154
Haucke, M., Cidale, L. S., Venero, R. O. J., et al. 2018, A&A, 614, A91
Kaufer, A., Stahl, O., Wolf, B., et al. 1996, A&A, 314, 599
Klein, R. I., & Castor, J. I. 1978, ApJ, 220, 902
Kramida, A., Ralchenko, Yu., Reader, J., & NIST ASD Team 2018, NIST Atomic Spectra Database (ver. 5.6.1), [Online]. Available: https://physics.nist.gov/asd (Gaithersburg, MD: National Institute of Standards and Technology)
Kraus, M., Haucke, M., Cidale, L. S., et al. 2015, A&A, 581, A75
Kudritzki, R.-P., & Puls, J. 2000, ARA&A, 38, 613
Kurucz, R. L. 1979, ApJS, 40, 1
Lefever, K., Puls, J., & Aerts, C. 2007, A&A, 463, 1093
Lenorzer, A., Vandenbussche, B., Morris, P., et al. 2002, A&A, 384, 473
Lenorzer, A., Mokiem, M. R., de Koter, A., & Puls, J. 2004, A&A, 422, 275
Lenz, P., & Breger, M. 2005, Commun. Asteroseismol., 146, 53
Lépine, S., & Moffat, A. F. J. 2008, AJ, 136, 548
Lovekin, C. C., & Guzik, J. A. 2014, MNRAS, 445, 1766
Lucy, L. B., & Solomon, P. M. 1970, ApJ, 159, 879
Maharramov, Y. M. 2013, Astron. Rep., 57, 303
Markova, N., Prinja, R. K., Markov, H., et al. 2008, A&A, 487, 211
Meynet, G., Chomienne, V., Ekström, S., et al. 2015, A&A, 575, A60
Mihalas, D. 1967, ApJ, 149, 169
Mihalas, D. 1978, Stellar atmospheres (San Francisco: W.H. Freeman)
Mihalas, D., & Kunasz, P. B. 1978, ApJ, 219, 635
Morel, T., Marchenko, S. V., Pati, A. K., et al. 2004, MNRAS, 351, 552
Morris, P. W., Eenens, P. R. J., Hanson, M. M., Conti, P. S., & Blum, R. D. 1996, ApJ, 470, 597
Najarro, F., Hanson, M. M., & Puls, J. 2011, A&A, 535, A32
Newville, M., Stensitzki, T., Allen, D. B., & Ingargiola, A. 2014, https://zenodo.org/record/11813
Newville, M., Stensitzki, T., Allen, D. B., et al. 2016, Astrophysics Source Code Library, [record ascl:1606.014]
Ng, Y. J. 1974, PhD thesis, Harvard University, Massachusetts (USA)
Oksala, M. E., Kraus, M., Cidale, L. S., Muratore, M. F., & Borges Fernandes, M. 2013, A&A, 558, A17
Owocki, S. P., Castor, J. I., & Rybicki, G. B. 1988, ApJ, 335, 914
Pauldrach, A., Puls, J., & Kudritzki, R. P. 1986, A&A, 164, 86
Prinja, R. K., Rivinius, T., Stahl, O., et al. 2004, A&A, 418, 727
Puls, J., Markova, N., Scuderi, S., et al. 2006, A&A, 454, 625
Puls, J., Vink, J. S., & Najarro, F. 2008, A&Ar, 16, 209
Repolust, T., Puls, J., Hanson, M. M., Kudritzki, R.-P., & Mokiem, M. R. 2005, A&A, 440, 261
Saio, H., Georgy, C., & Meynet, G. 2013, MNRAS, 433, 1246
Simón-Díaz, S., Uytterhoeven, K., Herrero, A., Castro, N., & Puls, J. 2010, Astron. Nachr., 331, 1069
Smith, N. 2014, ARA&A, 52, 487
Sundqvist, J. O., Björklund, R., Puls, J., & Najarro, F. 2019, A&A, 632, A126
Taylor, W. D., Evans, C. J., Simón-Díaz, S., et al. 2014, MNRAS, 442, 1483
Venero, R. O. J., Curé, M., Cidale, L. S., & Araya, I. 2016, ApJ, 822, 28
Yadav, A. P., & Glatzel, W. 2016, MNRAS, 457, 4330
Zaal, P. A., Waters, L. B. F. M., Geballe, T. R., & Marlborough, J. M. 1997, A&A, 326, 237
Zaal, P. A., de Koter, A., Waters, L. B. F. M., et al. 1999, A&A, 349, 573
Zaal, P. A., de Koter, A., & Waters, L. B. F. M. 2001, A&A, 366, 241